

CrystEngComm

Accepted Manuscript



This is an *Accepted Manuscript*, which has been through the Royal Society of Chemistry peer review process and has been accepted for publication.

Accepted Manuscripts are published online shortly after acceptance, before technical editing, formatting and proof reading. Using this free service, authors can make their results available to the community, in citable form, before we publish the edited article. We will replace this *Accepted Manuscript* with the edited and formatted *Advance Article* as soon as it is available.

You can find more information about *Accepted Manuscripts* in the [Information for Authors](#).

Please note that technical editing may introduce minor changes to the text and/or graphics, which may alter content. The journal's standard [Terms & Conditions](#) and the [Ethical guidelines](#) still apply. In no event shall the Royal Society of Chemistry be held responsible for any errors or omissions in this *Accepted Manuscript* or any consequences arising from the use of any information it contains.

Effects of morphology, size and crystallinity on the electrochromic properties of nanostructured WO₃ films

Feng Zheng^{a,b,c}, Wenkuan Man^a, Min Guo^{*,a}, Mei Zhang^a, Qiang Zhen^{b,c}

Abstract: WO₃ nanostructures with various morphologies and crystallinity (such as cylinder-like WO₃ nanorod arrays (WNRs-1), porous WO₃ nanofibers, WO₃ nanoflake arrays, sharp cone-like nanorod arrays (WNRs-2) and annealed cylinder-like WNRs-1) were prepared on FTO substrates by using a hydrothermal method without organic additives. The effects of morphology, size and crystallinity on the electrochromic properties of WO₃ nanostructures were systematically investigated by scanning electron microscopy, X-ray diffraction, cyclic voltammetry and chronoamperometry. The WNRs-1 exhibited excellent cyclic stability, wide optical modulation (64%), and relatively high coloration efficiency (61 cm² C⁻¹). A fast switching speed of 5 s and 6 s for bleaching and coloration are achieved for the WNRs-1 after annealing. Moreover, the relationship between the micro-morphologies/structures and electrochromic performance of WO₃ nanostructures was also discussed.

^a State Key Laboratory of Advanced Metallurgy, School of Metallurgical and Ecological Engineering, University of Science and Technology Beijing, Beijing 100083, P. R. China

^b Materials Science and Engineering college, Shanghai University, Shanghai 200444, P. R. China

^c Nano-science and Nano-technology Research Center, School of Materials Science and Engineering, Shanghai University, Shanghai 200444, P.R. China

* E-mail address: guomin@ustb.edu.cn, Fax: +86 10 62334926

1. Introduction

WO₃ is an indirect semiconductor with an adjustable band gap of 2.5-3.65 eV¹ and has been extensively used in many fields such as solar cell², photocatalyst³, gas sensor^{4,5}, and especially electrochromic (EC) device^{6,7}. By alternately applying a small positive and negative voltage, WO₃ can switch reversibly between colorless and blue color due to its electrochemical double injection/extraction of Li-ions and electrons into/out of the host lattice of WO₃. It is known that the coloration/bleaching response speed of WO₃ is limited both by the interface reaction process⁸ between the WO₃ and electrolyte, as well as the ions diffusion process⁹ in the WO₃ crystal lattice. The former depends on the morphology of the formed WO₃, and the later is mainly determined by the crystallinity of synthesized WO₃. In addition, the optical modulation rests with the Li-ions storage capacity of WO₃, which mainly depends on the size and crystalline of formed WO₃.

In recent years, the EC properties of WO₃ nanostructures with different morphologies have been widely studied. Ou¹⁰ et al. synthesized highly ordered 3D WO₃ nanoporous networks on FTO by using an electrochemical anodization method. The 3D WO₃ nanoporous networks with its superior active surface area demonstrated excellent coloration efficiency (CE, 141.5 cm² C⁻¹). Jiao¹¹ et al. prepared 2D Plate-like 3WO₃·H₂O film on FTO via a hydrothermal method. The film exhibited a fast coloration/bleaching response (4.3 s /1.4 s) and a high CE value (112.7 cm² C⁻¹), which were ascribed to a large surface area. Ma¹² et al. fabricated vertically aligned 1D WO₃ nanostructure films on FTO using a hydrothermal technique. Due to the 1D ordered structure, a large optical modulation of 66%, fast coloration and bleaching times of 6.7 s and 3.4 s, and a high CE of 106 cm² C⁻¹ were achieved for the cylindrical nanorod array film. Although a lot of literatures have reported different morphologies of WO₃ nanostructures and their EC properties, most of them focus on specific morphology. The relationship between the morphologies and EC performance parameters is still one of the most challenging issues.

In addition, as for the effect of WO_3 crystal structures on the EC properties, Maruyama¹³ et al. synthesized amorphous WO_3 thin films on FTO by chemical vapor deposition, the CE of $230 \text{ cm}^2 \text{ C}^{-1}$ was obtained and it was hard to be overtaken. However, Lee⁸ et al. fabricated crystalline WO_3 nanostructures on FTO by a hot-wire chemical-vapor-deposition process. They found that the crystalline WO_3 nanostructures have greater charge density, comparable CE and excellent cycling stability compared with amorphous WO_3 films. Till now, the effect of crystal form and crystalline degree on the EC properties of WO_3 nanostructures is controversial.

In this paper, we study the effect of the morphologies, sizes and crystallinity on the EC properties of nanostructured WO_3 films. The cycling stability, optical modulation, responding time and coloration efficiency of different WO_3 nanostructures, such as cylinder-like WO_3 nanorod arrays (WNRs-1), porous WO_3 nanofibers, WO_3 nanoflake arrays, sharp cone-like WO_3 nanorod arrays (WNRs-2) and annealed WNRs-1 were studied in detail. And we establish the correlation between the micro-morphologies/structures and EC performance parameters of WO_3 nanostructures.

2. Experimental sections

2.1. Materials

All chemicals (Beijing Chemicals Reagent Company) were of analytical reagent grade and used without further purification. All the aqueous solutions were prepared using double distilled and ion-exchanged water. Fluorine doped Tin Oxide (FTO, $10\text{-}15 \Omega \text{ cm}^{-2}$) glass plates were used as substrates and were cleaned by standard procedures prior to use.

2.2. Substrate pre-treatment

Preparation of H_2WO_4 colloid solution for coating substrates was described as follows: tungstic acid powder (H_2WO_4 , 0.01 mol) was dissolved into hydrogen peroxide solution (H_2O_2 , 20 mL, 30 wt %) to yield a homogeneous and stable colloid. Then the colloid solution was dropped onto $4.5 \times 1.0 \text{ cm}^2$

FTO substrate for spin-coating (KW-4A, made by Chinese Academy of Sciences) and annealing (SX₂-4-10, made by Tianjin Zhonghuan Experimental Furnace Co., Ltd.). The spin-coating process was performed at 3000 rpm for 30 s and the annealing processes were heated at 500 °C. These processes were recycled for 3 times, both of the previous two annealing processes were performed for 10 min and the last time for 30 min. After these processes the FTO substrate covered with WO₃ seed layers was obtained.

2.3. Hydrothermal synthesis

Vertically aligned WNRs-1 was fabricated by a typical hydrothermal technique. The precursor solution was prepared as follows: sodium tungstate dihydrate powder (Na₂WO₄•2H₂O, 0.025 mol) was dissolved in distilled water (25 mL). Then the final pH value of the precursor solution was adjusted by the following two steps. Firstly, the pH value of the solution was acidified to 2.0 with hydrochloric acid (HCl, 2 mol L⁻¹) by magnetic stirring, and white precipitate was generated. Secondly, the solution was diluted to 250 mL and oxalic acid (H₂C₂O₄) was added to the mixture to adjust the final pH value to 2.0. After stirred for 30 min, 30 mL of the precursor solution was transferred into a 50 mL Teflon-lined autoclave and Rubidium Sulfate (Rb₂SO₄, 3.75×10⁻³ mol) was added to it. Then the hydrothermal growth was carried out at 180 °C for 4 h in a sealed Teflon-lined autoclave by immersing the FTO substrate with the WO₃ seed layers in the precursor solution. After the reaction finished, the autoclave was cooled to room temperature naturally. Subsequently, the as-deposited substrate was rinsed repeatedly with deionized water and dried in air for further characterization.

We note that using the same general synthesis technique, different morphologies of WO₃ nanostructures (porous WO₃ nanofibers and WO₃ nanoflake arrays) were synthesized by modification of the WNRs-1 hydrothermal conditions. For the porous WO₃ nanofibers, the final pH value of the precursor solution was adjusted to 2.4, and the reaction was kept at 160 °C for 4 h with

potassium chloride (KCl, 7.5×10^{-3} mol) as capping agent. For the WO₃ nanoflake arrays, the final pH value of the precursor solution was adjusted to 1.5, and the reaction was kept at 180 °C for 40 min with sodium chloride (NaCl, 7.5×10^{-3} mol) as capping agent. In addition, to investigate the effect of sizes on the EC properties of WO₃ nanorod arrays, Larger sizes of sharp cone-like WO₃ nanorod arrays (WNRs-2) were fabricated as follows: the final pH value of the precursor solution was adjusted to 2.4, and the reaction was kept at 170 °C for 2 h with NaCl (7.5×10^{-3} mol) as capping agent. To investigate the effect of crystallinity degree on the EC properties of WO₃ nanorod arrays, the WNRs-1 were annealed in air at 500 °C for 1 h.

2.4. Characterization

The morphologies and crystal phase of the WO₃ nanostructures were characterized by scanning electron microscopy (SEM, Zeiss, Supra-55) and X-ray diffraction (XRD, Rigaku Dmax-2500). Cyclic voltammetry (CV) measurements were performed on an electrochemical workstation (VMP3, Princeton Applied Research) using a three-electrode system in a beaker with 80 mL (1 mol L⁻¹ LiClO₄ in propylene carbonate (PC)) electrolyte. The FTO substrate with the WO₃ nanostructures, a Pt wire and an Ag/AgCl electrode were used as working, counter and reference electrodes, respectively. Chronoamperometry of the WO₃ nanostructures by applying voltages of ± 3.0 V for 300 s and in situ measurement of the WO₃ films with voltage step between -3.0 V (100 s) and +3.0 V (100 s) were carried out on an electrochemical workstation (CHI660C, Shanghai Chenhua Instrument, Inc.) in a colorimetric cell (1.0 cm² × 4.2 cm) with 3 mL (1 mol L⁻¹ LiClO₄ in PC) electrolyte. The transmittance spectra were measured using a UV-vis spectrophotometer (TU-1901, Beijing Purkinje General Instrument Co., Ltd.) in the spectral region between 360 and 800 nm by chronoamperometry. The in situ coloration/bleaching switching characteristics were recorded using a UV-vis spectrophotometer with a wavelength of 600 nm.

3. Results and discussion

3.1. Effect of morphology and size on the electrochromic properties

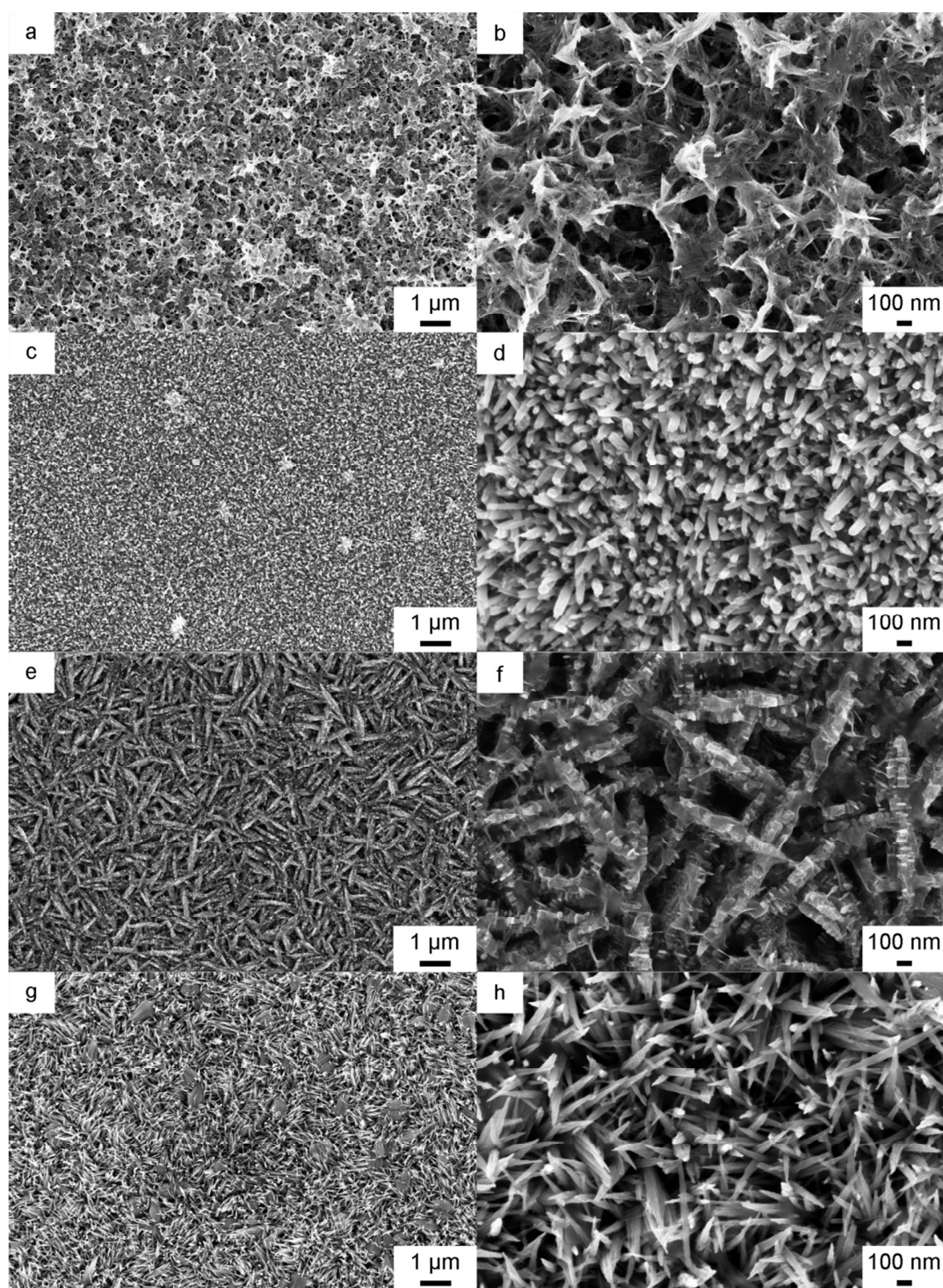


Fig. 1 SEM images of (a) and (b) porous WO₃ nanofibers, (c) and (d) WNRs-1, (e) and (f) WO₃ nanoflake arrays, (g) and (h) WNRs-2.

To investigate the effect of morphology on the EC properties of WO_3 nanostructures, three different kinds of nanostructured WO_3 films were synthesized by hydrothermal method. Fig. 1 shows the SEM images of different morphologies of WO_3 nanostructures grown on FTO substrates. The porous WO_3 film is composed of a large number of nanofibers with small diameter. These nanofibers agglomerate together and stack disorderly, with porous and interconnected network structures (Fig. 1a and b). From Fig. 1c, well aligned WNRs-1 grow vertically in a large scale. The nanorods are about 50-80 nm in diameter with top-down structures as shown in Fig. 1d. For the WO_3 nanoflake arrays (Fig. 1e and f), the average length of the nanoflakes is 1 μm , with a thickness of 100 nm. These nanoflakes arrange disorderly, resulting in the formation of pores among these nanoflakes. In addition, it can be seen that these nanoflakes are composed of nanoparticles at high magnification in Fig. 1f. To further demonstrate the effect of the sizes on the electrochromic properties of the nanostructured WO_3 films, we therefore adjusted the precursor solution and the capping agent to obtain larger sizes of sharp cone-like WNRs-2. It is found from the Fig. 1g and h that the main products are nanorods with larger diameters (80-120 nm) and tapering structures generally vertical to the substrates mixed with a few spindle-like nanorod bundles. According to the reports in literatures¹⁴⁻¹⁶, all of these nanostructured WO_3 films have high surface area, which could facilitate the Li-ions to intercalate into/deintercalate out of the WO_3 crystal lattice.

Fig. 2 shows the corresponding XRD patterns of WO_3 nanostructures with different morphologies and sizes on FTO substrates. Except for the peaks of FTO glass, the diffraction peaks of all the films can be indexed as the hexagonal WO_3 phase (JCPDS 01-085-2459). The pattern of porous WO_3 nanofibers have high background noise and large full width at half maximum (FWHM), indicating the porous WO_3 nanofibers have low crystallinity and small size. For the WNRs-1, the (002) peak is significantly enhanced compared with the other samples, suggesting that the WNRs-1 have preferential growth direction along the c-axis [001]. As for WO_3 nanoflake arrays, the

relatively stronger diffraction peaks and smaller FWHM indicate the good crystallinity and large sizes of the prepared samples. It is also noted that the (002) diffraction peak can hardly be found and the intensities of the diffraction peaks of the (110), (200) and (220) crystal planes, which are vertical to the (001) crystal system, are much higher than those of other peaks. Thus, it can be inferred that the WO_3 nanoflake arrays possess preferential growth direction almost parallel to the substrate. Although the three samples also have differences on the crystallinity, the most obvious differences are their morphologies. From the typical XRD pattern of WNRs-2 in Fig. 2d, the FWHM is narrow and the background noise is weak compared with the WNRs-1, indicating better crystallinity or larger sizes of the as-prepared sample. In addition, the (002) crystal plane relative intensity of WNRs-2 is lower than that of the WNRs-1, which might be ascribed to that a few spindle-like nanorod bundles existed in the WNRs-2, resulting in decreased (002) crystal plane as the top face of the WNRs-2. All the results of XRD patterns in Fig. 2 are consistent with the SEM images in Fig. 1.

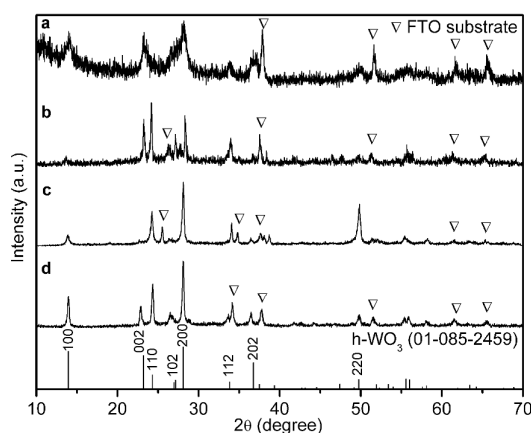


Fig. 2 XRD patterns of (a) porous WO_3 fibers, (b) WNRs-1, (c) WO_3 nanoflake arrays, (d) WNRs-2.

Generally, the characteristic parameters of WO_3 for EC properties are the cycling stability, optical modulation, responding times, and coloration efficiency. It is indicated that one of the most important factors for EC properties is the cycling stability. Usually, the cyclic voltammograms (CVs) is used to elucidate the cycling stability of WO_3 . Fig. 3 shows the CVs of the four WO_3

nanostuctures between -1.0 and 1.0 V at a scan rate of 50 mV s⁻¹ for different cycles. As can be seen from the CVs, these WO₃ films give a pair of redox peaks which can be ascribed to the intercalation/deintercalation of both Li-ions and electrons into/out of the WO₃ crystal lattice, represented as the following reaction^{17,18}:



It is found that no significant change in the shape of CVs appears during the periods of 1000th cycles in Fig. 3b, c, and d, suggesting excellent cycling stability of the WNRs-1, WO₃ nanoflake arrays and WNRs-2. However, the current density of the porous WO₃ nanofibers decreases slowly from the first cycle to the 1000th cycle as shown in Fig. 3a. This difference might be mainly attributed to the effect of the morphologies and sizes, that is to say, the WO₃ nanofibers with small sizes cause them to dissolve into the electrolyte slightly faster than the nanorods and nanoflakes with large sizes.

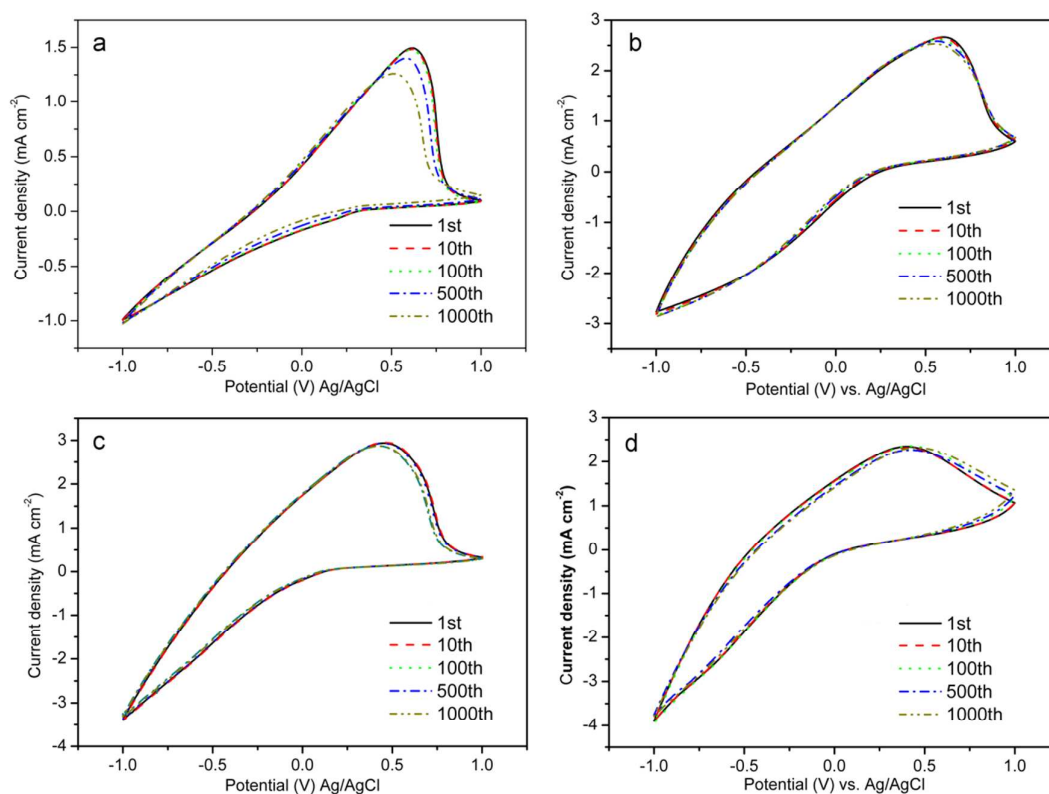


Fig. 3 The cyclic voltammograms of (a) porous WO₃ fibers, (b) WNRs-1, (c) WO₃ nanoflake arrays, (d) WNRs-2.

Li-ions charge/discharge densities (intercalation/deintercalation of Li-ions) calculated from the CVs are 18.6/18.4, 51.9/48.2, 51.2/49.8 and 56.1/53.7 mC cm^{-2} for the porous WO_3 nanofibers, WNRs-1, WO_3 nanoflake arrays and WNRs-2, respectively, which are taken as a representation of the Li-ions storage capacity. Obviously, the Li-ions storage capacities of the WNRs-1, WO_3 nanoflake arrays and WNRs-2 are much larger than that of the porous WO_3 nanofibers, suggesting that the nanostructures with larger size have higher Li-ions storage capacity. In addition, the cyclic reversible values could reach as high as 99% (WO_3 nanofibers), 93% (WNRs-1), 97% (WO_3 nanoflake arrays) and 95% (WNRs-2) calculated from intercalation/deintercalation of Li-ions charge/discharge densities, may be ascribed to the higher surface area of the porous structures (WO_3 nanofibers and WO_3 nanoflake arrays) and top-down structures^{19,20} (WNRs-1 and WNRs-2). These reversibility values are largely increased compared with the reported ones of the WO_3 nanoporous network¹⁰ (85-93%) and nanocuboids²¹ (72%).

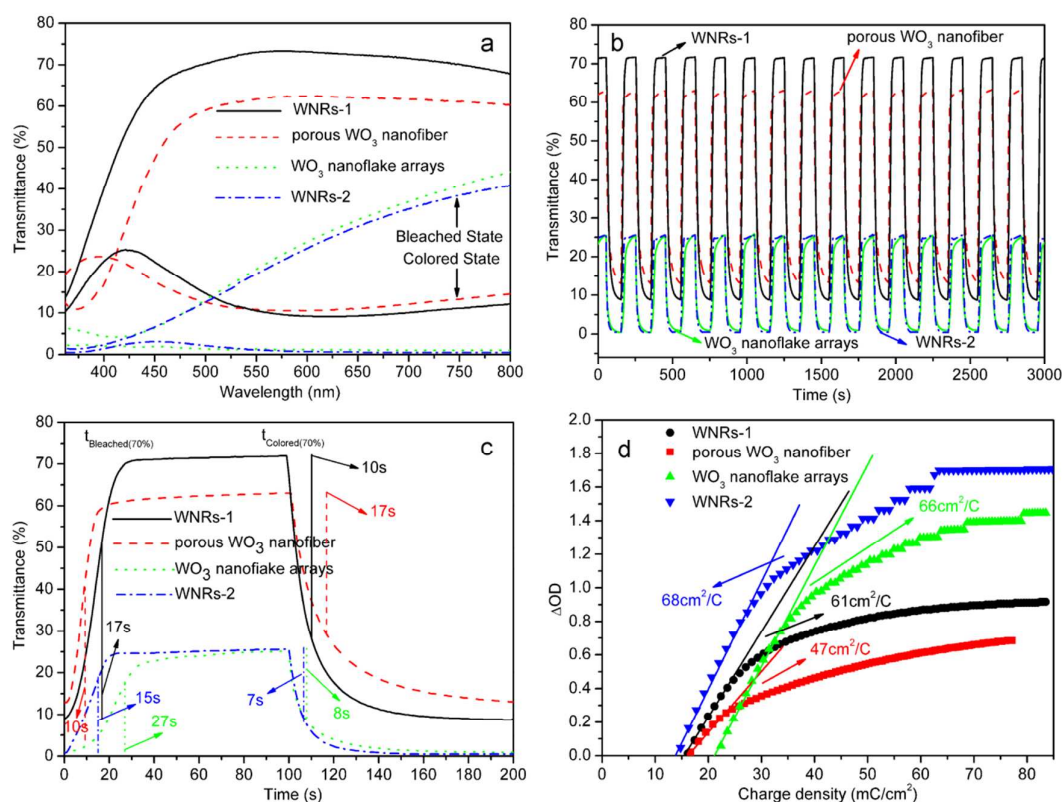


Fig. 4 Electrochromic properties of WO_3 nanostructures with different morphologies and sizes: (a) UV-vis

transmittance spectra at colored and bleached state ± 3.0 V for 300 s; (b, c) switching time characteristics between

the colored and bleached states measured at ± 3.0 V with a wavelength of 600 nm; (d) coloration efficiency at 600 nm.

The maximum optical modulation is defined as the maximum difference between the transmittance of WO_3 film at colored and bleached states in the visible region. Chronoamperometry of the WO_3 nanostructures by applying voltages of ± 3.0 V for 300 s is carried out in 3 mL electrolyte (1 mol L^{-1} LiClO_4 in PC) to investigate the optical modulation. The corresponding UV-vis transmittance spectra recorded in the wavelength range of 360–800 nm are shown in Fig. 4a. It can be clearly seen that the maximum optical modulation of coloration/bleaching at 600 nm is about 64% for WNRs-1, while the minimum optical modulation of coloration/bleaching at 600 nm is about 24% for WNRs-2 and nanoflake arrays, further confirming that different morphologies and sizes of WO_3 nanostructures resulting in different optical modulations. In order to compare the switching characteristics among the four different morphologies and sizes of WO_3 nanostructures, in situ transmittance curves at 600 nm of these samples are shown in Fig. 4b and c. From Fig. 4b, it can be seen that the cyclic reversibility of the four samples are stable after a series of cycles, which are consistent with the results from the CVs in Fig. 3. The maximum/minimum optical transmittances of bleaching/coloration are found to be 63%/13% (porous WO_3 fibers), 72%/8% (WNRs-1) and 25%/1% (WO_3 nanoflake arrays and WNRs-2) at 600 nm after applying a ± 3.0 V voltage biasing for 100 s, respectively, which correspond to the transmittance curves in Fig. 4a.

The coloration and bleaching times are extracted as the time required for 70% in the whole transmittance modulation at 600 nm in Fig. 4c. For the porous WO_3 nanofibers, the coloration time of $t_{c(70\%)}$ is found to be 17 s while the bleaching time $t_{b(70\%)}$ is about 10 s. This means that the Li-ions are easier to deintercalate out of than intercalate into the crystal lattice of the porous WO_3 nanofibers, which is in accordance with the cyclic reversible values (99%). For the WNRs-1 and WO_3 nanoflake arrays, the coloration/bleaching times are 10 s/17 s and 8 s/27 s, respectively,

suggesting that the Li-ions are easier to intercalate into the crystal lattice of the WNRs-1 and WO₃ nanoflake arrays by applying a negative voltage, while the Li-ions require a process to get out when a positive voltage is applied. This phenomenon could be explained as follows: generally, the coloring process contains the interface reaction process and the ions diffusion process. With the action of the concentration gradients of Li-ions and the electric field force, firstly, the Li-ions migrate to the surface of the WO₃ nanostructures from the electrolyte, and then the Li-ions inject into the WO₃ crystal lattice. At the same time, the electrons transfer to the WO₃ crystal lattice and combine with Li-ions to form LiWO₃ through the conductive substrate. The discoloring process is a reverse process of the coloring process. As for the porous WO₃ nanofibers, at the coloration stage, the Li-ions storage capacity could be easier saturated because of the small sizes of the WO₃ nanofibers. Then, the subsequent Li-ions are difficult to get into the crystal lattice of the WO₃ nanofibers. Conversely, at the bleaching stage, the Li-ions are easy to get out of the WO₃ nanofibers, which have short diffusion paths in the crystal lattice and between the WO₃ and electrolyte attributed to the small size, porous and network structures. For the WNRs-1 and nanoflake arrays, the average sizes of the nanostructures are greater than that of the WO₃ nanofibers. By applying a negative voltage, both the concentration gradient force of Li-ions and the electric field force could promote Li-ions to get into the crystal lattice of the WO₃ nanostructures from electrolyte. And the h-WO₃ could accommodate abundant Li-ions due to its three possible locations²² (trigonal cavity, hexagonal window and four-coordinated square window). However, when a positive voltage is applied, the direction of concentration gradient force of Li-ions is the reverse of the electric field force, and the opposite forces could reach an equilibrium state, leading to that part of Li-ions still remain in the WO₃ crystal lattice. These results agree well with the cyclic reversible values 93% (WNRs-1) and 97% (WO₃ nanoflake arrays) calculated from CVs in Fig. 3b and c. So the responding time is largely dependent on the size. The larger the size of the WO₃ nanostructures is,

the shorter the coloration time and the longer the bleaching time will be. In addition, it is found that porous WO_3 nanofiber and WNRs-1 show much lower resistance than that of the WO_3 nanoflake arrays at bleaching state (Fig. S1), indicating the fast charge transfer and Li^+ ion diffusion resulting in fast switching kinetics. The coloration and bleaching time of the WNRs-2 with larger size are 7 s and 15 s, respectively, which further prove this point. Fig. 5 shows the interface reaction process of Li-ions and electrons between the WO_3 and electrolyte and their diffusion process in the WO_3 crystal lattice. Furthermore, the responding time of the WNRs-1 are faster than the compact assembled nanorod films prepared by drop-assembly, which need 25 s and 18 s for a 70% modulation in coloration and bleaching, respectively²³. The fast switching speed of the WNRs-1 is due to the large active surface area, top-down structure, and good contact between the nanorods and the substrate.

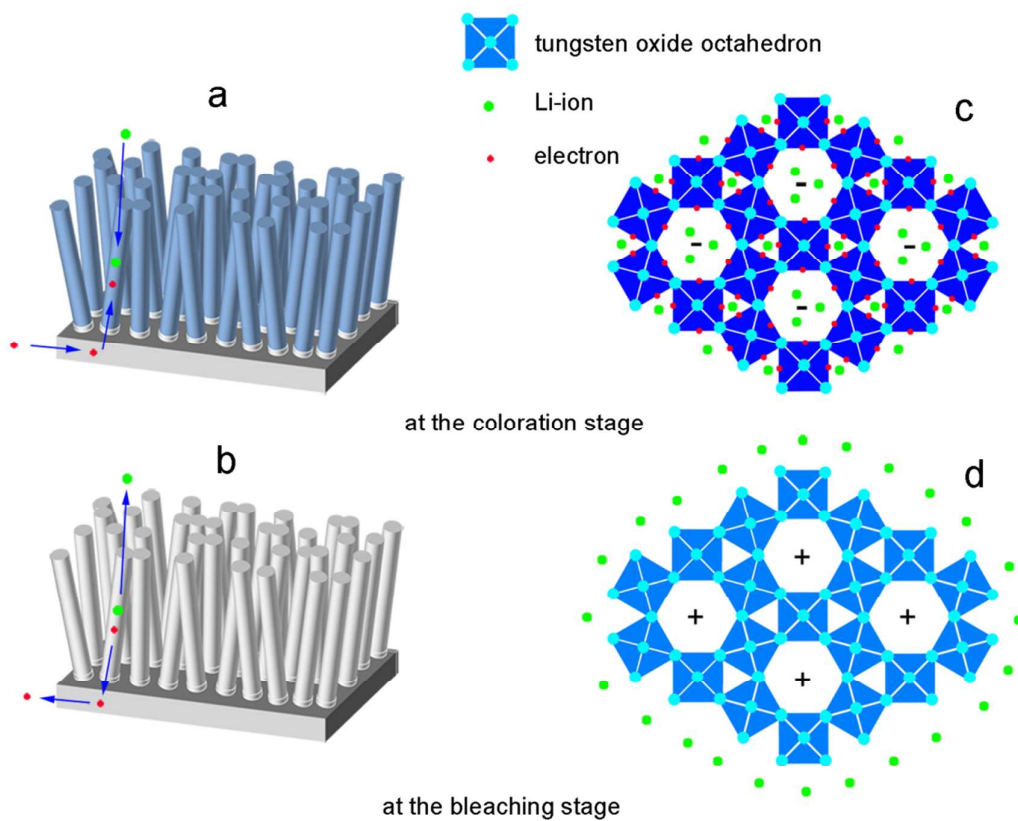


Fig. 5 The electrochromic mechanism of the WNRs (a, b) the interface reaction process of Li-ions and electrons between the WO_3 and electrolyte; (c, d) the diffusion process of Li-ions in the WO_3 crystal lattice.

In addition, it is demonstrated that another key factor for EC properties is the coloration efficiency of WO_3 , which is defined as the change in optical density (OD) per unit of charge density (Q/A) during switching and can be calculated according to the formula: $CE = \Delta OD / (Q/A)^{24,25}$, where $OD = \log(T_b/T_c)$, T_b and T_c refer to the transmittance of the film in its bleached and colored states, respectively. Fig. 4d shows the plots of OD at a wavelength of 600 nm vs. the inserted charge density at a potential of -3.0 V. The CE values are extracted as the slope of the lines fit to the linear region of the curves. The calculated CE value for the porous WO_3 nanofibers is $47 \text{ cm}^2 \text{ C}^{-1}$, which is lower than that of the WNRs-1 ($61 \text{ cm}^2 \text{ C}^{-1}$) and WO_3 nanoflake arrays ($66 \text{ cm}^2 \text{ C}^{-1}$). These values are in the range of efficiencies reported for other nanostructured WO_3 films ($32\text{-}151.9 \text{ cm}^2 \text{ C}^{-1}$)²⁶⁻³¹. Generally, it is believed that a high value of CE indicates that the electrochromic materials exhibits large optical modulation with small charge inserted. From Fig. 4a and b, it is verified that the transmittance modulation of the WNRs-1 is larger than that of the porous WO_3 nanofibers. So, the WNRs-1 has a larger CE value than that of the porous WO_3 nanofibers in Fig. 4d. Though the transmittance modulation of the WO_3 nanoflake arrays is relatively smaller compared with that of the WNRs-1, the CE value of the former is comparable to that of the later. We could find the reason from the formula: $OD = \log(T_b/T_c)$, as for the WO_3 nanoflake arrays, the values of T_c (Fig. 4c) as the denominators are relatively smaller than those of the other two WO_3 nanostructures with different morphologies at the same time. Then the WO_3 nanoflake arrays could acquire a series of higher OD values which result in a higher value of CE. From these experiments, it is found that reducing the T_c values can also improve the CE value of the electrochromic materials. The CE value of the WNRs-2, which has the response curve (Fig. 4c) analogous to the WO_3 nanoflake arrays, can reach a relative higher value ($68 \text{ cm}^2 \text{ C}^{-1}$) for further proof.

Based on above analysis, the WNRs-1 have enhanced electrochromic properties compared with other WO_3 nanostructures due to their appropriate sizes, large surface areas, ordered

arrangements and top-down structures, which provide more capability for accommodating the Li-ions and direct paths for the process of Li-ions intercalation/deintercalation.

3.2. Effect of crystallinity on the electrochromic properties

To study the crystallinity of the WO_3 nanostructures affects their electrochromic properties, the WNRs-1 were annealed at $500\text{ }^\circ\text{C}$ for 1 h. The surface topography of the annealed WNRs-1 was observed by SEM (Fig. 6). It is found that the nanorods are still very stable and their morphologies did not appear significant change. Unlike the morphologies shown in Fig. 1c and d, the annealed nanorods become angular with clear edges. This may be because the annealing process lead to higher degree of crystallinity.

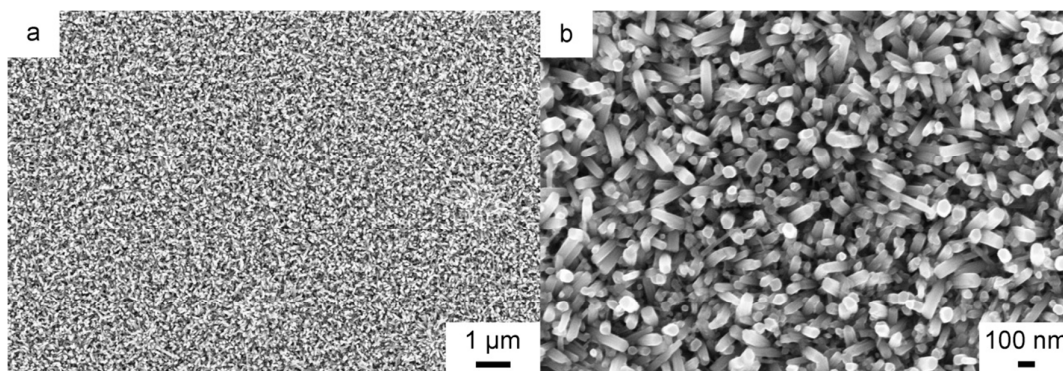


Fig. 6 SEM images of (a) and (b) WNRs-1 annealed at $500\text{ }^\circ\text{C}$ for 1 h.

Fig. 7 shows the XRD patterns of the WNRs-1 annealed at $500\text{ }^\circ\text{C}$ for 1 h. Besides the peaks from the FTO substrate, the products not only contains hexagonal- WO_3 (JCPDS 01-085-2459), but also monoclinic- $\text{W}_{18}\text{O}_{49}$ (JCPDS 01-071-2450), indicating that crystal transformation occurs during the annealing process. It might be because the unannealed products contain small amounts of H_xWO_3 , namely, the H-ions intercalate into the crystal lattice of the hexagonal WNRs-1. After annealing, the crystal water is removed from the crystal lattice of H_xWO_3 , and then WO_{3-x} is generated which is the monoclinic- $\text{W}_{18}\text{O}_{49}$ detected from the XRD pattern.

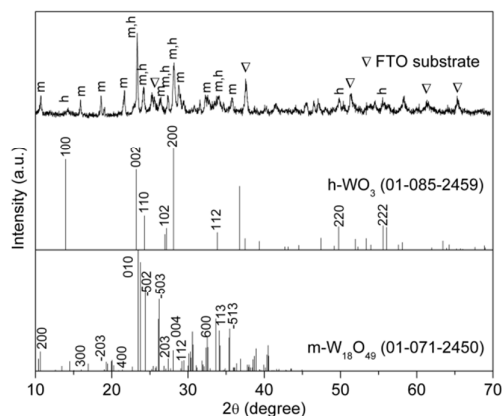


Fig. 7 XRD pattern of WNRs-1 annealed at 500 °C for 1 h.

Typical cyclic voltammogram for annealed WNRs-1 is shown in Fig. 8. Unlike the curves in Fig. 3, the annealed WNRs-1 shows two distinct redox couples, suggesting that there might be two couples of intercalation/deintercalation of Li-ions and electrons into/out of the WO_{3-x} , represented as the following reactions³²:

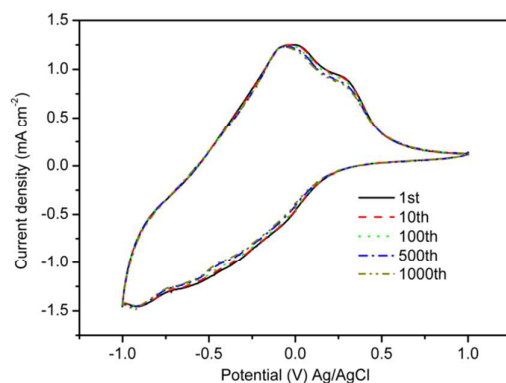


Fig. 8 The cyclic voltammograms of WNRs-1 annealed at 500 °C for 1 h.

The two couples of redox peaks are in accordance with two sets of tungsten oxide compounds (hexagonal- WO_3 and monoclinic- $\text{W}_{18}\text{O}_{49}$) in Fig. 7. The repetitive cycling between the bleached and colored states of the annealed WNRs-1 shows good stability after 1000 cycles, implying that the crystal size is the main factor for cycling stability. In addition, the annealed WNRs-1 shows relative lower charge/discharge densities of 27.1 mC cm^{-2} (in the intercalation) and 19.3 mC cm^{-2} (in

the deintercalation) compared with the unannealed WNRs-1, which may be closely related to the different crystalline forms. The h-WO₃ could accommodate abundant Li-ions due to its three possible locations (trigonal cavity, hexagonal window and four-coordinated square window). However, when the h-WO₃ is translated to m-W₁₈O₄₉, a large amount of hexagonal windows disappear which result in low capacity for Li-ions. Moreover, the cyclic reversible value is only 71% calculated from the charge/discharge densities, which is mainly ascribed to the oxygen deficiency. Greater oxygen deficiency in W₁₈O₄₉ could capture a certain amount of electrons in the deintercalation. Furthermore, this experiment has settled the disputes of electrochromic mechanism between the double injection model³³ and the small polaron model³⁴. A major focus of the debate is the valence transformation of tungsten element in the color-changed process. The double injection model suggested that the valence transformation of tungsten element changed between plus five and plus six. While the small polaron model believed that it should be between plus five and plus four. From Fig. 8, we know that there indeed is a mixture of two kinds of valence changes in the annealed WNRs-1 during the charging and discharging process.

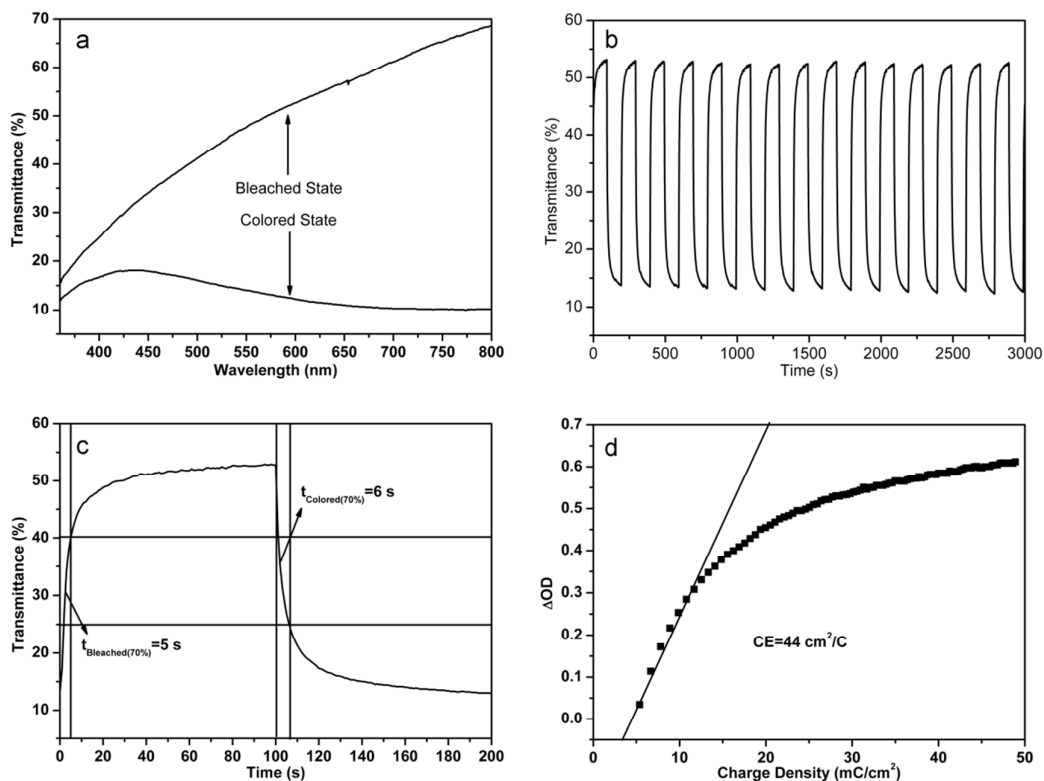


Fig. 9 Electrochromic properties of WNRs-1 annealed at 500 °C for 1 h: (a) UV-vis transmittance spectra at colored and bleached state ± 3.0 V for 300 s; (b, c) switching time characteristics between the colored and bleached states measured at ± 3.0 V with a wavelength of 600 nm; (d) coloration efficiency at 600 nm.

Fig. 9 shows the electrochromic properties of the WNRs-1 annealed at 500 °C for 1 h. Transmittance spectra of the annealed WNRs-1 in colored and bleached states are displayed in Fig. 9a. The annealed WNRs-1 exhibits an obvious transmittance difference in the visible light range with a maximum contrast of 59% at 800 nm. For the purpose of comparison, the in situ coloration/bleaching switching of the annealed WNRs-1 was measured at 600 nm, as shown in Fig. 9b and c. The optical modulation contrast of coloration/bleaching is found to be 40% at 600 nm after applying a ± 3.0 V voltage biasing for 100 s, respectively, which corresponds to the transmittance study in Fig. 9a. The optical modulation contrast of annealed WNRs-1 at 600 nm is smaller than that of the unannealed WNRs-1 (64%), which is also attributed to the decreasing of the hexagonal windows. In addition, for the annealed WNRs-1, the coloration/bleaching time is found to be 6 s and 5 s, respectively, which is much faster than that of the unannealed WNRs-1, indicating

that the Li-ions and electrons are easier to intercalate into/deintercalate out of the crystal lattice. This case may be ascribed to the increased crystallinity degree which may offer low resistance for ions and electrons transport. The calculated CE of the annealed WNRs-1 is $44 \text{ cm}^2 \text{ C}^{-1}$, which is the lowest in all of as-prepared samples. Fig.10 shows the electrochromic schematic diagram of monoclinic $\text{W}_{18}\text{O}_{49}$. Table 1 concludes the characteristic parameters of different morphology, size and crystallinity of nanostructured WO_3 films for EC properties. Based on the above analysis, the hexagonal- WO_3 have higher Li-ions storage capacity, larger optical modulation and higher CE values attributed to its hexagonal windows, and high crystallinity degree of WO_3 nanostructures have faster responding times due to its low resistance for ions and electrons transport.

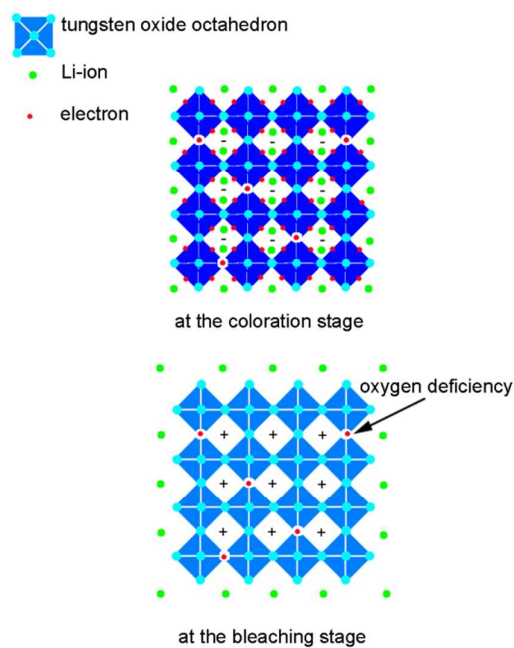


Fig.10 The electrochromic schematic diagram of monoclinic $\text{W}_{18}\text{O}_{49}$.

Table 1 The characteristic parameters of different morphology, size and crystallinity of nanostructured WO_3 films for EC properties: (a) porous WO_3 nanofibers, (b) WNRs-1, (c) WO_3 nanoflake arrays, (d) WNRs-2, (e) annealed WNRs-1.

	Porous WO ₃ nanofibers	WNRs-1	WO ₃ nanoflake arrays	WNRs-2	annealed WNRs-1
Charge densities (mC cm ⁻²)	18.6	51.9	51.2	56.1	27.1
Discharge densities (mC cm ⁻²)	18.4	48.2	49.8	53.7	19.3
Cyclic reversible values	99%	93%	97%	95%	71%
Optical transmittances at bleaching state (@600 nm)	63%	72%	25%	25%	53%
Optical transmittances at coloration state (@600 nm)	13%	8%	1%	1%	13%
Optical modulation (@600 nm)	50%	64%	24%	24%	40%
Coloration time (t _(70%) , s)	17	10	8	7	6
Bleaching time (t _(70%) , s)	10	17	27	15	5
Coloration efficiency (cm ² C ⁻¹)	47	61	66	68	44

4、 Conclusion

In summary, we have prepared WO₃ nanostructures with different morphologies and crystallinity on FTO substrates by using a hydrothermal method without organic additives. It is shown that the size of nanostructured WO₃ films play an important role in electrochromic properties. The porous WO₃ nanofibers have poor cycling stability, long coloration time and low coloration efficiency mainly due to their smaller sizes. Conversely, the WO₃ nanoflake arrays have low optical modulation and long bleaching time, which is attributed to their larger sizes. The WNRs-1 have enhanced electrochromic properties compared with porous WO₃ nanofibers and WO₃ nanoflake arrays due to

their appropriate sizes, large surface areas, ordered arrangements and top-down structures, which provide more capability for accommodating the Li-ions and direct paths for the process of Li-ions intercalation/deintercalation. From the effects of crystallinity on the electrochromic properties, the unannealed WNRs-1 has high optical modulation compared with the annealed WNRs-1, due to the large tunnels in the hexagonally structured WO_3 . The annealed WNRs-1 has short responding time which is ascribed to the high crystalline degree.

Acknowledgment

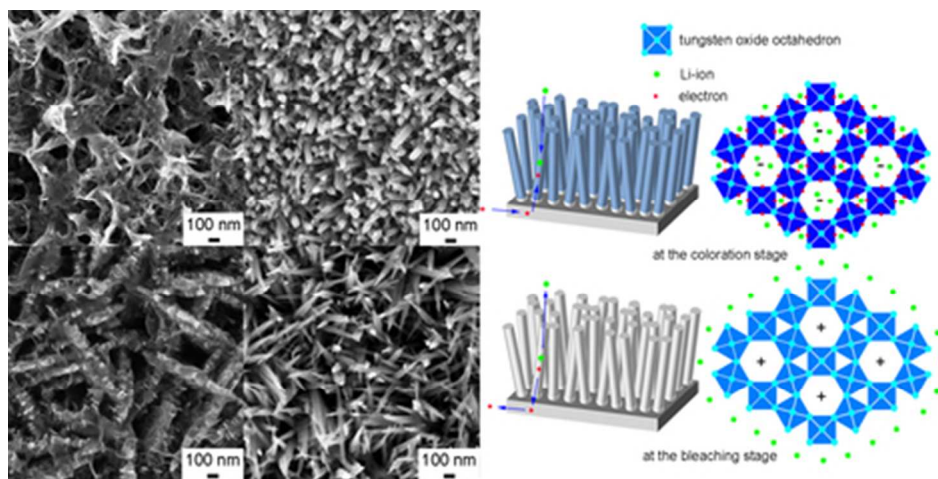
The work is supported by the National Nature Science Foundation of China (No. 51272025, 50872011, 50672006 and 51472156).

References

- 1 I. Turyan, U. O. Krasovec, B. Orel, T. Saraidorov, R. Reisfeld and D. Mandler, *Adv. Mater.*, 2000, 12, 330-333.
- 2 H. Zheng, Y. Tachibana and K. Kalantar-zadeh, *Langmuir*, 2010, 26, 19148-19152.
- 3 L. Zhang, Y. Li, Q. Zhang and H. Wang, *CrystEngComm*, 2013, 15, 5986-5993.
- 4 H. Zhang, M. Yao, L. Bai, W. Xiang, H. Jin, J. Li and F. Yuan, *CrystEngComm*, 2013, 15, 1432-1438.
- 5 S. Bai, K. Zhang, X. Shu, S. Chen, R. Luo, D. Li and A. Chen, *CrystEngComm*, 2014, 16, 10210-10217.
- 6 M. Layani, P. Darmawan, W. L. Foo, L. Liu, A. Kamyshny, D. Mandler, S. Magdassi and P. S. Lee, *Nanoscale*, 2014, 6, 4572-4576.
- 7 G. Cai, J. Tu, D. Zhou, L. Li, J. Zhang, X. Wang and C. Gu, *CrystEngComm*, 2014, 16, 6866-6872.
- 8 S. H. Lee, R. Deshpande, P. A. Parilla, K. M. Jones, B. To, A. H. Mahan and A. C. Dillon, *Adv. Mater.*, 2006, 18, 763-766.

- 9 B. Kattouf, G. L. Frey, A. Siegmann and Y. E. Eli, *Chem. Commun.*, 2009, 7396-7398.
- 10 J. Z. Ou, S. Balendhran, M. R. Field, D. G. McCulloch, A. S. Zoolfakar, R. A. Rani, S. Zhuiykov, A. P. O'Mullane and K. Kalantar-zadeh, *Nanoscale*, 2012, 4, 5980-5988.
- 11 Z. Jiao, X. Wang, J. Wang, L. Ke, H. V. Demir, T. W. Koh and X. W. Sun, *Chem. Commun.*, 2012, 48, 365-367.
- 12 D. Ma, G. Shi, H. Wang, Q. Zhang and Y. Li, *J. Mater. Chem. A*, 2013, 1, 684-691.
- 13 T. Maruyama and S. Arai, *J. Electrochem. Soc.*, 1994, 141, 1021-1024.
- 14 B. Kattouf, Y. E. Eli, A. Siegmann and G. L. Frey, *J. Mater. Chem. C*, 2013, 1, 151-159.
- 15 J. Yang, W. Li, J. Li, D. Sun and Q. Chen, *J. Mater. Chem.*, 2012, 22, 17744-17752.
- 16 S. S. Kalanur, Y. J. Hwang, S. Y. Chae and O. S. Joo, *J. Mater. Chem. A*, 2013, 1, 3479-3488.
- 17 J. Wang, E. Khoo, P. S. Lee and J. Ma, *J. Phys. Chem. C*, 2008, 112, 14306-14312.
- 18 J. Zhang, J. Tu, G. Du, Z. Dong, Y. Wu, L. Chang, D. Xie, G. Cai and X. Wang, *Sol. Energy Mater. Sol. Cells*, 2013, 114, 31-37.
- 19 H. Hu, H. Cheng, G. Li, J. Liu and Y. Yu, *J. Mater. Chem. A*, 2015, 3, 2748-2755.
- 20 J. Zhang, W. Zhang, Z. Yang, Z. Yu, X. Zhang, T. C. Chang and A. Javey, *Sens. Actuators B*, 2014, 202, 708-713.
- 21 S. Adhikari and D. Sarkar, *RSC Adv.*, 2014, 4, 20145-20153.
- 22 S. Balaji, Y. Djaoued, A. S. Albert, R. Z. Ferguson and R. Bruning, *Chem. Mater.*, 2009, 21, 1381-1389.
- 23 J. Wang, E. Khoo, P. S. Lee and J. Ma, *J. Phys. Chem. C*, 2009, 113, 9655-9658.
- 24 D. Ma, G. Shi, H. Wang, Q. Zhang and Y. Li, *J. Mater. Chem. A*, 2014, 2, 13541-13549.
- 25 Y. C. Her and C. C. Chang, *CrystEngComm*, 2014, 16, 5379-5386.
- 26 K. Wang, P. Zeng, J. Zhai and Q. Liu, *Electrochem. Commun.*, 2013, 26, 5-9.
- 27 C. P. Li, F. Lin, R. M. Richards, C. Engtrakul, R. C. Tenent and C. A. Wolden, *Sol. Energy*

- Mater. Sol. Cells*, 2014, 121, 163-170.
- 28 G. F. Cai, J. P. Tu, D. Zhou, X. L. Wang and C. D. Gu, *Sol. Energy Mater. Sol. Cells*, 2014, 124, 103-110.
- 29 Z. Jiao, J. Wang, L. Ke, X. Liu, H. V. Demir, M. F. Yang and X. W. Sun, *Electrochimica Acta*, 2012, 63, 153-160.
- 30 V. V. Kondalkar, S. S. Mali, R. R. Kharade, K. V. Khot, P. B. Patil, R. M. Mane, S. Choudhury, P. S. Patil, C. K. Hong, J. H. Kim and P. N. Bhosale, *Dalton Trans.*, 2015, 44, 2788-2800.
- 31 V. V. Kondalkar, S. S. Mali, R. R. Kharade, R. M. Mane, P. S. Patil, C. K. Hong, J. H. Kim, S. Choudhury and P. N. Bhosale, *RSC Adv.*, 2015, 5, 26923-26931.
- 32 S. H. Lee, H. M. Cheong, J. G. Zhang, A. Mascarenhas, D. K. Benson and S. K. Deb, *Appl. Phys. Lett.*, 1999, 74, 242-244.
- 33 S. H. Lee, H. M. Cheong, P. Liu, D. Smith, C. E. Tracy, A. Mascarenhas, J. R. Pitts and S. K. Deb, *Electrochimica Acta*, 2001, 46, 1995-1999.
- 34 J. G. Zhang, D. K. Benson, C. E. Tracy, S. K. Deb and A. W. Czanderna, *J. Electrochem. Soc.*, 1997, 144, 2022-2026.



Hydrothermal preparation of different morphologies of nanostructured WO₃ films and the electrochromic mechanism of the WO₃ nanorod arrays.
39x19mm (300 x 300 DPI)